Optical Observation Regions in Cislunar Space Using the Bi-Circular Restricted Four Body Problem Geometry

Surabhi Bhadauria and Carolin Frueh
School of Aeronautics and Astronautics, Purdue University
sbhadaur@purdue.edu,cfrueh@purdue.edu

ABSTRACT

The number of missions into the cislunar realm, the space from the Earth to including the lunar region, is about to increase in the foreseeable future. This development also imposes a need for space domain awareness (SDA) in this spatial domain. Objects of interest include active spacecraft and space debris alike. The cislunar region is vast, and its dynamics are rich, which allows for a plethora of possible orbits with an almost infinite parameter space for surveillance scenarios. Testing single orbits at specific epochs can only offer point solutions. When observing optically, the problem is inevitably time-dependent, even when using simplifying assumptions for the orbital dynamics. In this paper, the bi-circular restricted four-body problem (BCR4BP) is leveraged to mark regions of higher and lower visibility with observers and objects throughout the entire cislunar region. Point solutions are avoided entirely in this approach. In this parameterization, the parameter space can be explored with minimal computational cost and be visualized in the natural periods of the cislunar four-body system. This approach offers unique insights for SDA observation constellation planning and space object tracking in the Cislunar domain.

1. INTRODUCTION

With the increasing number of planned and actual missions significantly beyond the geostationary ring, the need for Space Domain Awareness (SDA) has expanded into the entire Cislunar region [1]. Cislunar denotes the region of space between the Earth and the Moon, sometimes also denoted as XGEO. A plethora of different orbits, trajectories, and orbital structures exist in Cislunar space because it deviates from a regime that can be well-approximated in the two-body model. As a result, the parameter space to explore and develop SDA solutions is vast. A number of authors have explored optical observation conditions and surveillance options with space-based or ground-based observers [2, 3, 4, 5, 6, 7, 8, 9, 10, 11, 12, 13], sensor tasking [14, 15, 11] and orbit determination [8, 16, 17, 18, 19]: Point solutions of specific orbits at specific times and observation conditions have been explored, and expansion to more generalized solutions has proven challenging [13]. While orbit design often occurs in the Circular Restricted Three-Body Problem (CR3BP)[20, 5, 6, 18, 13, 19], the optical illumination conditions ultimately render the problem time-dependent. As a result, it is not possible to analyze the observation system solely using the simplified dynamics and advantageous parameterization of the - per construction time-independent - CR3BP. Full high-precision ephemerides models for the celestial bodys' locations and accurate models for non-conservative perturbing forces, such as solar radiation pressure (SRP), offer the most accurate orbit propagation for single scenarios. But those point solutions cannot readily be expanded into more global statements. However, formulating the constellation design, sensor tasking, and observation strategies as an optimization problem requires a suitable parametrization [11, 7, 21, 15]; the computational demands of the chosen parameterization dictate the ease of finding optimal or near-optimal solutions.

This paper explores the parametrization provided by the Bi-Circular Restricted Four Body Problem (BCR4BP) [22, 23, 24, 25, 26, 27, 28]. The BCR4BP is a time-dependent approximation that offers a parametrization significantly simpler than the pointwise integration of an ephemerides model in Cartesian space. The BCR4BP has traditionally not been used for calculations in the Cislunar space. The influence of the Sun's gravity is negligible in a first-order approximation in the Cislunar regime and can easily be corrected when transferring a solution from the CR3BP into the high-fidelity ephemerides propagation model. However, the BCR4BP offers a formulation that includes the movement of the Sun, which is crucial for representing the illumination conditions for passive optical observers in the Cislunar realm and beyond. In this paper, a general formulation of the Cislunar optical SDA surveillance problem is derived leveraging the BCR4BP, determining region of high and low observation count. Preliminary analyses using the same method have been published by the same authors previously [29].

2. BI-CIRCULAR RESTRICTED FOUR BODY PROBLEM (BCR4BP) FORMULATION

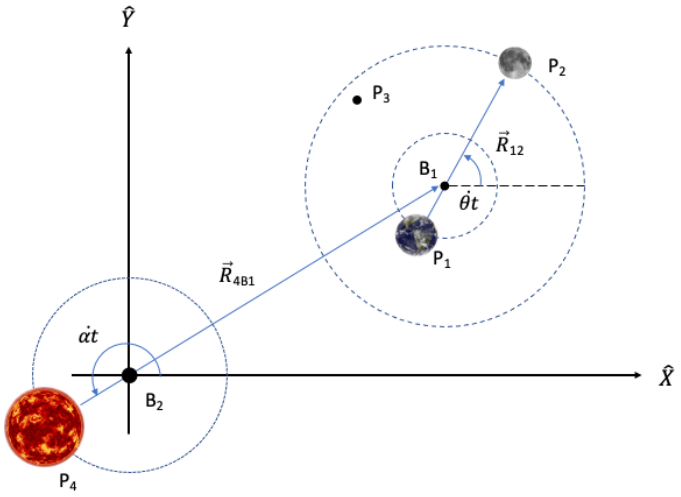

Fig. 1: In-plane BCR4BP model in the Sun-Moon-Earth system [28]: P_1 denotes the Earth location, P_2 the Moon, P_3 the satellites and B_1 the Earth-Moon barycenter. P_4 is the location of the Sun; B_2 denotes the Sun-Earth-Moon barycenter. The assumption of the orbits of the bodies is indicated with blue dashed circles. Note, the angles $\dot{\alpha}t$ for the motion of the Sun in P_4 is defined with respect to the inertial $\hat{X}$ direction with the origin in B_2 and the angle $\dot{\theta}t$ is defined for the motion of the Moon with respect to the inertial $\hat{X}$ direction with origin in B_2 .

First introduced in 1960 [22], the BCR4BP approximates the system dynamics of a small body subject to three major bodies, such as a satellite in the Earth-Moon-Sun system [22, 23]. The BCR4BP schematics is illustrated in Fig. 1 [28] for the Earth-Moon-Sun system. The first two bodies, located at P_1 and P_2 with masses m_1 and m_2, in our case denoting the Earth and the Moon, form together with the small body, e.g. a satellite at P_3 with mass m_3 the CR3BP, with $m_1 > m_2 >> m_3$. Moon and Earth are on circular orbits around their common Earth-Moon barycenter, located at B_1; the angle between the lunar direction to the inertial reference direction $\hat{X}$-axis (e.g., the vernal equinox) is denoted by $\dot{\theta}t$, where t denotes time. In the BCR4BP, there is a fourth body located at P_4 with $m_4 > m_3$. In our case, the fourth body is the Sun. The Sun and the Earth-Moon system are in circular orbits around the Sun-Earth-Moon barycenter, denoted by B_2. The angle between the solar direction to the inertial reference direction with origin in B_2 is denoted by $\dot{\alpha}t$. All celestial bodies, Sun and the Earth-Moon system, are assumed to be in a common plane in the planar formulation of the BCR4BP [23] used in this paper.

Let the vectors $\vec{R}_{B_1 1}$ and $\vec{R}_{B_1 2}$ denote the position vector of the Earth and the Moon from the Earth-Moon barycenter B_1, respectively. They can, hence, be expressed as the following:

$$\vec{R}_{B_1 1} = |\vec{R}_{B_1 1}|(-\cos(\dot{\theta}t + \theta_0)\hat{X} - \sin(\dot{\theta}t + \theta_0)\hat{Y}), \tag{1}$$

$$\vec{R}_{B_1 2} = |\vec{R}_{B_1 2}|(\cos(\dot{\theta}t + \theta_0)\hat{X} + \sin(\dot{\theta}t + \theta_0)\hat{Y}), \tag{2}$$

where θ_0 refers to the angle angle between the lunar direction to the inertial reference direction $\hat{X}$ at the initial epoch. Accordingly, the vectors denoted by $\vec{R}_{B_2 4}$, pointing from the system's barycenter B_2 to the Sun is:

$$\vec{R}_{B_2 4} = |\vec{R}_{B_2 4}|(\cos(\dot{\alpha}t + \alpha_0)\hat{X} + \sin(\dot{\alpha}t + \alpha_0)\hat{Y}), \tag{3}$$

$$\tag{4}$$

where α_0 refers to the angle angle between the lunar direction to the inertial reference direction $\hat{X}$ at the initial epoch.

The vectors from barycenter B_2 to the barycenter B_1 denoted by $\vec{R}_{B_2B_1}$ can be expressed as:

$$\vec{R}_{B_2B_1} = |\vec{R}_{B_2B_1}|(-\cos(\dot{\alpha}t+\alpha_0)\hat{X} - \sin(\dot{\alpha}t+\alpha_0)\hat{Y}), \tag{5}$$

$$\tag{6}$$

And the position of the Earth-Moon barycenter B_1 relative to the Earth, $\vec{R}_{1B_1}$, can then be written as:

$$\vec{R}_{1B_1} = |\vec{R}_{B_1 1}|(\cos(\dot{\theta}t+\theta_0)\hat{X} + \sin(\dot{\theta}t+\theta_0)\hat{Y}). \tag{7}$$

The position of the Moon from the Earth, $\vec{R}_{12}$, is:

$$\vec{R}_{12} = \vec{R}_{1B_1} + \vec{R}_{B_1 2} = |\vec{R}_{12}|(\cos(\dot{\theta}t+\theta_0)\hat{X} + \sin(\dot{\theta}t+\theta_0)\hat{Y}). \tag{8}$$

Similarly, the position of the Sun from the Earth, $\vec{R}_{14}$, is:

$$\vec{R}_{14} = \vec{R}_{1B_1} + \vec{R}_{B_1B_2} + \vec{R}_{B_2 4} = |\vec{R}_{B_1 1}|(\cos(\dot{\theta}t+\theta_0)\hat{X} + \sin(\dot{\theta}t+\theta_0)\hat{Y}) + |\vec{R}_{B_1 4}|(\cos(\dot{\alpha}t+\alpha_0)\hat{X} + \sin(\dot{\alpha}t+\alpha_0)\hat{Y}). \tag{9}$$

The object's position P_3 can be varied in two parameters - the angle from the inertial axis, $\dot{\phi}t$, and the distance from the barycenter B_1, $|\vec{R}_{B_1 3}|$ to cover the entire cislunar space. Therefore, the position of the object to Earth, $\vec{R}_{B_1 3}$, is:

$$\vec{R}_{B_1 3} = |\vec{R}_{B_1 3}|(\cos(\dot{\theta}t+\theta_0+\delta_3)\hat{X} + \sin(\dot{\theta}t+\theta_0+\delta_3)\hat{Y}), \tag{10}$$

where δ_3 is the excess angle of the object at P_3 relative to the Moon's location, an out-of-plane angular component can be readily added.

3. OBSERVATION CONDITIONS AND CONSTRAINTS

The conditions and constraints of relevance in optical observation scenarios can easily be expressed in terms of angular relations using the BCR4BP and the parameterization from Eqs.2-10.

The observed magnitude, m_{object}, of a spherical Lambertian object with reflectivity C_d and radius R is computed as the following

$$\begin{aligned} m_{\text{object}} &= m_{\text{sun}} - 2.5\log(\frac{I_{\text{object}}}{I_{\text{sun}}}), \\ I_{\text{object}} &= \frac{I_{\text{sun}}}{d}\frac{c_d R^2}{\pi}\frac{2}{3}(\sin(\psi) + (\pi-\psi)\cos(\psi)), \end{aligned} \tag{11}$$

where m_{sun} is the reference magnitude of the Sun, I_{object} is the irradiation of the object at the location of the observer, and I_{sun} is the irradiation of the Sun at the object's location. The d denotes the distance between the object and the observer. Th angle ψ denotes the phase angle of the observation geometry between the Sun, the object, and the observer.

In the simplest terms, a magnitude limit can be defined to evaluate an observation scenario. More realistically, a probability of detection formulation is used based on the telescope parameters of optics, camera, celestial background sources and detector noises [30, 31, 32, 33, 34].

An observer in the Cislunar region at location P_5 relative to the barycenter B_1 can now be expressed as:

$$\vec{R}_{B_1 5} = |\vec{R}_{15}|(\cos(\dot{\theta}t+\theta_0+\delta_5)\hat{X} + \sin(\dot{\theta}t+\theta_0+\delta_5)\hat{Y}), \tag{12}$$

where δ_5 is the excess angle of the object at P_5 relative to the Moon's location, an out-of-plane angular component for $\vec{R}_{B_1 5}$ can be readily added. Hence, the following expression is found for the phase angle ψ:

$$\cos\psi = \frac{\vec{R}_{35}\cdot\vec{R}_{34}}{|\vec{R}_{35}||\vec{R}_{34}|}. \tag{13}$$

Defining simple avoidance conditions can be a useful tool when it is evident that background sources overpower the reflected signal of an object.

The angle between the object's position and the Sun, β, and angle between the object's position and the Moon, γ, relative to the observer can hence be expressed as:

$$\cos\beta = \frac{\vec{R}_{53} \cdot \vec{R}_{54}}{|\vec{R}_{53}||\vec{R}_{54}|} \tag{14}$$

$$\cos\gamma = \frac{\vec{R}_{53} \cdot \vec{R}_{52}}{|\vec{R}_{53}||\vec{R}_{52}|} \tag{15}$$

While those equations are not surprising per se the Sun and Moon exclusion angles and the phase angle can easily be computed by simple angular quantities in the BCR4BP parametrization. The computations of the entire illumination conditions are hence, very computationally efficient.

4. OBSERVATION CONDITION EVALUATION

The BCR4BP is, of course, an approximation. Validations with high-fidelity ephemerides models have been performed for spherical objects, where the out-of-plane component of the illumination is negligible [29]. A good agreement within a timeframe of several months has been found.
In order to quantify how often an object in a given region of space is visible to an observer i located at x_i, y_i, a simple visibility count percentage ($VCP_{\text{single},i}$) measure has been defined: Stepping through a given time horizon the account of successful visibility t_{visible} is contrasted by the number of all possible visibility occasions t_{all}:

$$VCP_{\text{single},i} = \frac{t_{\text{visible},i}}{t_{\text{all}}} \times 100. \tag{16}$$

Visibility is assessed using user-defined criteria of the probability of detection or a magnitude limit in combination with the Sun, the Moon, and the Earth exclusion angles, which may be evaluated for one or more given object sizes and albedo assumptions. Because of the discretization, the cut-off effects occur but are negligible for small time steps between subsequent visibility checks.

A second measure that has been proven very useful in the analysis is to not only restrict to one or a small number of observers but also to discretize the cislunar region for a comprehensive distribution of all possible observers:

$$VCP_{\text{all}} = \sum_{i}^{n} \frac{t_{\text{visible},i}}{n} \times 100, \tag{17}$$

which means a score of 100 in the VCP_{all} corresponds to an object that would be visible to all observers during the entire time interval. Because of the low computational cost, even with small discretization steps, the VCP_{all} score is computed rapidly.

5. RESULTS

The analysis method shown here is simply a tool for more general statements at a meager computational cost. It allows more fully exploring the vast parameter space: a first step before point solutions for select cases in high-precision models are carried out.

The visibility measure assumes a limiting magnitude of 20 and a Sun, Earth, and Moon exclusion angle of 50, 30, and 35 degrees. For simplicity and to showcase the power of the method even with simplistic measures, no probability of detection measure is used, which would include sensitivity to zodiac light, observations through the Milky Way, and lunar phases, and avoids hard cut-offs [30, 31]. The objects are assumed to Lambertian spheres with radius of one meter and a Lambertian reflection coefficient of 0.5.

5.1 Single Space-Based Fixed Observer, All Objects: VCP_{single} for One Month

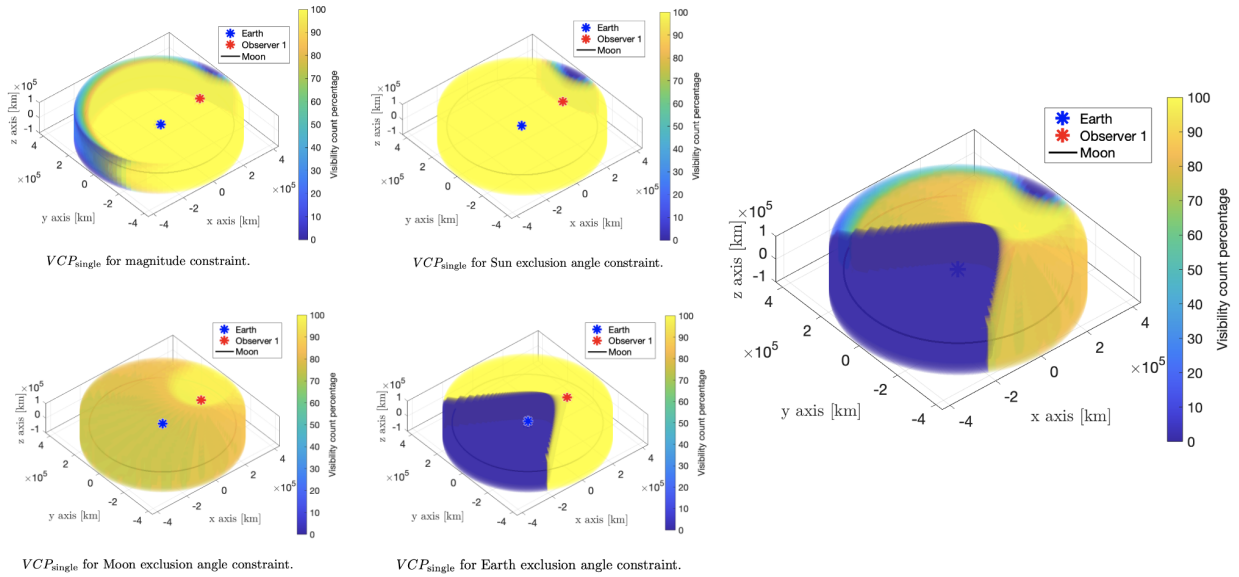

VCP_{single} for magnitude constraint.

VCP_{single} for Sun exclusion angle constraint.

VCP_{single} for Moon exclusion angle constraint.

VCP_{single} for Earth exclusion angle constraint.

Fig. 2: VCP_{single} for a one-month period with initial conditions of $\theta = 0$ and $\alpha = 0$: Magnitude constraint, Sun exclusion constraint, Moon exclusion constraint, and Earth exclusion constraint by themselves in the four plots on the left, and on the right for the combined constraints for a single observer marked by a red asterisk, for all objects within the cislunar region. The lunar orbit shines through in black.

In the first scenario, a single space-based observer is assumed. For the simulation, it has been placed more or less randomly in the cislunar plane. The VCP_{single} is computed for one month (corresponding, e.g., mid-March to mid-June, 2023), for initial conditions where both the Sun and Moon angle θ and α set out to be zero. Please note that while these conditions can be tied to actual times, the conditions repeat with the lunar and solar cycles. The repetition is exact in the BCR4BP and approximately in the real world. For the objects of interest, P_3, the entire cislunar plane, and out-of-plane locations have been simulated in an evenly spaced circular grid. The lunar orbit is shown as a black line in the plots; the objects have been extended beyond the Moon to capture far-side effects.

Fig.2 shows each of the influencing conditions by itself with its associated VCP_{single} over the course of the month. On the left: The visibility affected by the magnitude constraint and the sun exclusion angle constraint is shown in the top row. One can see that in a month, the Sun angle changes only over a small fraction of the cislunar region, excluding the direction directly towards the Sun for visibility, while at the same time favoring smaller phase angles in the magnitude constraint. Because the objects are assumed to be spherically shaped, larger phase angles still allow for good visibility. On the bottom row of Fig.2, the visibility for the Moon and the Earth exclusion angle constraints are shown. The Moon completes its orbit resulting in a more uniform pattern in the cislunar plane with significantly higher visibility around the observer location. The visibility for the Earth exclusion shows a strong directionality away from the Sun.

Fig.2 on the right in the larger plot, shows the true VCP_{single}, when all constraint displayed in Fig.2 are applied simultaneously. It can be seen that it is a simple superposition of all the constraints, with a large exclusion zone dominated by the Earth and a larger region of decreased but relatively high visibility with a favorable phase angle, which is infringed upon by the magnitude constraints and the Moon exclusion angle constraint.

5.2 All Observers, All Objects: VCP_{all} for One Month

In the following simulations, the VCP_{all} is computed, where the visibility for all objects and all observers is evaluated simultaneously. The simulation time is one month again.

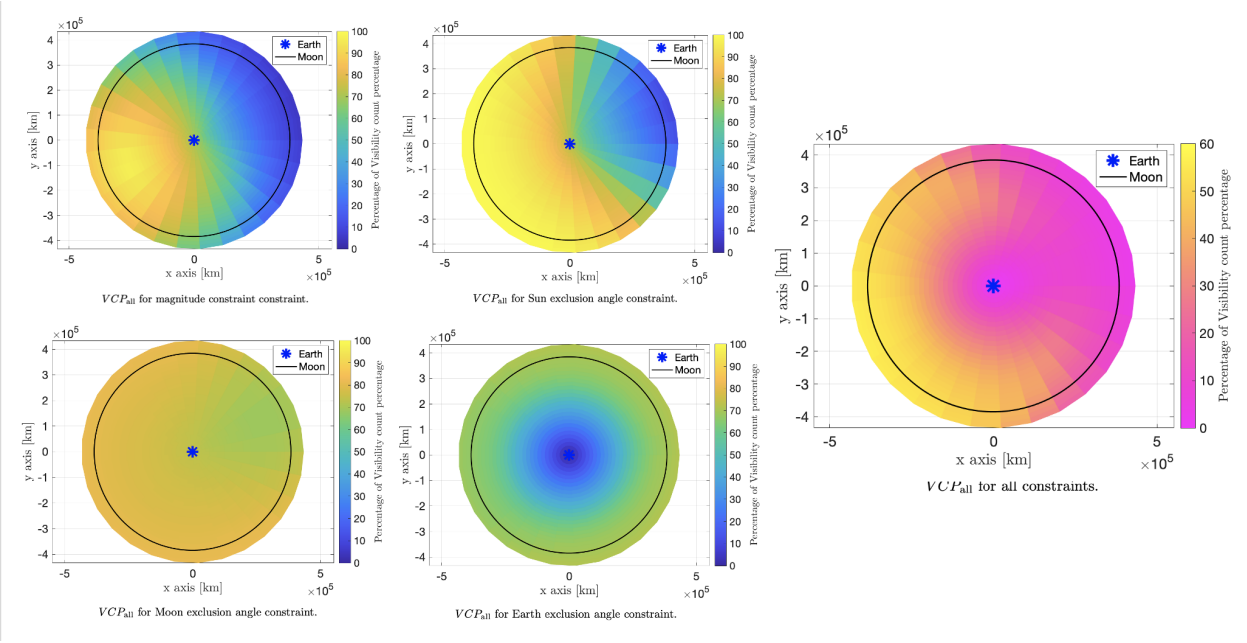

Fig. 3: VCP_{all} for a one-month period with initial conditions of $\theta = 0$ and $\alpha = 0$: Magnitude constraint, Sun exclusion constraint, Moon exclusion constraint, and Earth exclusion constraint by themselves in the four plots on the left, and on the right for the combined constraints for all objects and all observers within the Cislunar disk. The lunar orbit is marked in black.

5.2.1 Initial conditions $\alpha = 0$ Degrees Initial Angle with the Sun and $\theta = 0$ Degrees Initial Angle with the Moon

The identical initial conditions are used as for the single observer case in Section 5.1 to allow for a direct comparison.

Fig.3 shows the results for the VCP_{all} for the $\alpha = 0$ degrees initial angle with the Sun and $\theta = 0$ degrees initial angle with the Moon, e.g., corresponding to a mid-March to mid-June, 2023 scenario; again because of the periodicity, multiple periods are represented by the same scenario. This time, only the Cislunar plane itself is shown for enhanced clarity. On the top row left, one can see how the general visibilities directly tied to the Sun, magnitude and Sun exclusion angle, have not shifted fundamentally. They are less observer-dependent. However, significant changes can be observed in the bottom row with the Moon and Earth exclusion angle compared to a single observer, in Fig.2. In Fig.3, the strong tendency toward more visibility around the single observer location is gone. Instead, the region where the Moon passes twice (as the lunar period and one month do not align) is discernible with reduced visibility. The visibility affected by the Earth exclusion angle constraint, when considering all observers, is now completely symmetric, as expected. On the right in Fig.3, the visibility for all the constraints in combination is shown. Clearly, no location reaches a score of 100 anymore, which is not surprising, and a clear favoring of directions away from the Sun and away from the double lunar exclusion is discernible.

5.2.2 Comparison of Different Initial Conditions

The system in the BCR4BP has two exact periods, the synodic period of the Moon and the synodic period of the Sun, relative to the barycenters. As such, the time dependence of the BRC4BP parameterization shows differences in the monthly solutions, which Fig.4 illustrates: Different initial conditions for the monthly solutions are depicted. The chosen angles are $\alpha = 0, 90$ degrees for the angle of the Sun to the inertial $\hat{X}$ axis centered at B_2, and the angles $\theta = 0, 45, 270$ degrees for the lunar angle relative to the inertial $\hat{X}$ axis centered at B_1. The combination of $\alpha = 0$ and $\theta = 0$ has been explored in the previous sections and is just shown for comparison in the top left corner of Fig.4. Shifting just the solar angle α on the top right, compared to the top left, significantly changes the magnitude and solar

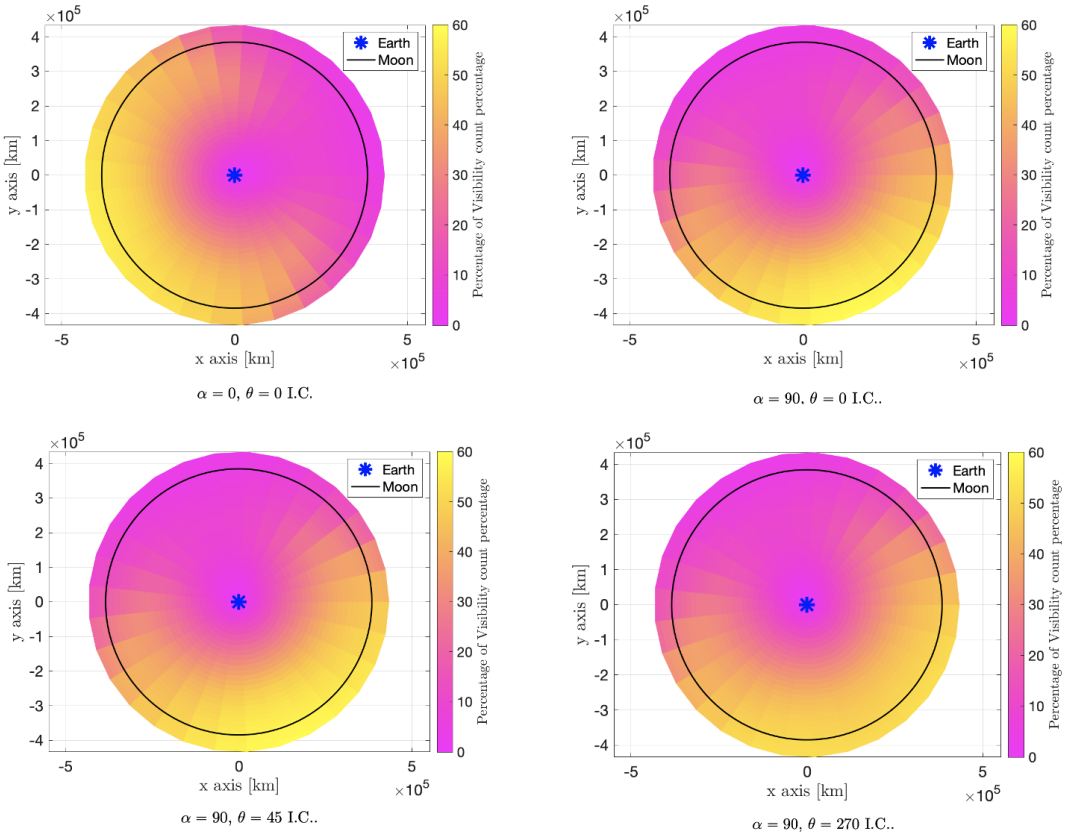

Fig. 4: VCP_{all} for a one-month period with all constraints applied for various initial conditions of the Sun initial angle α and the Moon initial angle of θ as initial conditions (I.C.).

exclusion angle constraints, leading to a shift of the highest visibility region shown in yellow colors. Keeping the solar angle α fixed and shifting just the lunar angle θ, comparing the top right plot with the bottom row plots, significantly affects the lunar exclusion angle. While the general location of the visibility stays nearly the same, the overall visibility is significantly lower in the $\theta = 270$ degree configuration on the bottom right, compared to the bottom left and top right with smaller lunar angles.

6. CONCLUSIONS

With an increased number of missions into the cislunar space significantly beyond the geosynchronous region, a need for space domain awareness of this larger space arises. Comprehensive surveillance with cost-efficient optical sensors is of specific interest. Because lunar gravity plays a significant role, two-body motion models are ill-suited. While orbits are often developed in the Circular Restricted Three Body Problem (CR3BP) parameterization using simplified dynamics, this parameterization does not represent all elements that influence the optical observation conditions. As a result, often, only the exploration of point solutions of specific orbits and specific conditions has been done because the parameter space is vast and cannot readily be explored comprehensively.

In this paper, the parameterization of the Bi-Circular Restricted Four Body Problem (BCR4BP), including not only Earth and Moon but also the Sun, has been explored. The BCR4BP parameterization offers a convenient way to express all observation conditions via angular relations that are easily computed and evaluated in a swift computational manner. The computational ease allows exploring the entire parameter space of observable objects in the cislunar plane. An observation measure has been developed to illustrate regions of high and low visibility given user-defined constraints of limiting magnitude and exclusion angle constraints for the Sun, the Earth, and the Moon. In a second step, the visibility measure is expanded to comprehensively compare the visibility of all objects vis-a-vie all possible observers. Several monthly solutions are explicitly shown.

The fast computation of the visibility count percentage allows for clearly discerning the influence of the various constraints on the overall visibility and discriminating regions of high and low visibility. It is shown that both the Sun and the Moon position alter the overall visibility scores and only their combined motion allows for a comprehensive review of the visibility conditions. The methodology offers insights that can inform point solution selections to be evaluated in a high-fidelity model.

7. ACKNOWLEDGMENTS

Many thanks go to Prof. Kathleen Howell, Maaninee Gupta, and Beom Park for their assistance.

REFERENCES

[1] M.J. Holzinger, C.C. Chow, and P. Garretson. *A Primer on Cislunar Space*. Air Force Research Laboratory, 2021.

[2] E. Fowler, S. Hurtt, and D. Paley. Observability metrics for space-based cislunar domain awareness. In *AAS/AIAA Astrodynamics Specialist Conference*, 2020.

[3] J Greaves and D Scheeres. Relative estimation in the cislunar regime using optical sensors. In *Advanced Maui Optical and Space Surveillance Technologies Conference. 22ND*, 2021.

[4] A.P. Wilmer, R.A. Bettinger, and B.D. Little. Preliminary viability assessment of cislunar periodic orbits for space domain awareness. In *2021 Advanced Maui Optical and Space Surveillance Technologies Conference (AMOS)*, 2021.

[5] C. Frueh, K. Howell, K. DeMars, and S. Bhadauria. Cislunar space situational awareness. In *31st AIAA/AAS Space Flight Mechanics Meeting*, 2021.

[6] C. Frueh, K. Howell, K. DeMars, S. Bhadauria, and M. Gupta. Cislunar space traffic management: Surveillance through earth-moon resonance orbits. In *8th European Conference on Space Debris*, 2021.

[7] M. Bolden, T. Craychee, and E. Griggs. An evaluation of observing constellation orbit stability, low signal-to-noise, and the too-short-arc challenges in the cislunar domain. In *Advanced Maui Optical and Space Surveillance Technologies Conference (AMOS)*, 2020.

[8] M. Thompson, C. Ré, N.and Meek, and B. Cheetham. Cislunar orbit determination and tracking via simulated space-based measurements. In *The Advanced Maui Optical and Space Surveillance Technologies (AMOS) Conference*, 2021.

[9] E. Plotke, P. Lai, A. Chan, R. Ewart, K. Miller, and J. Griesbach. Dual use star tracker and space domain awareness sensor in-space test. In *The Advanced Maui Optical and Space Surveillance Technologies (AMOS) Conference*, pages 14–17, 2021.

[10] P. Zimmer, J. McGraw, and M. Ackermann. Cislunar ssa/sda from the lunar surface: Cots imagers on commercial landers. In *The Advanced Maui Optical and Space Surveillance Technologies (AMOS) Conference*, 2021.

[11] G. Badura, Y. Shimane, K. Ho, A. Gregoire, B. Gunter, C. Valenta, M. Borowitz, J. Christian, and A. Sudol. System design and analysis for cislunar space domain awareness through distributed sensors. In *AAS/AIAA Astrodynamics Specialist Conference*, 2022.

[12] A. Wilmer J. Dahlke and R. Bettinger. Preliminary comparative assessment of l2 and l3 surveillance using select cislunar periodic orbits. In *AAS/AIAA Astrodynamics Specialist Conference*, 2022.

[13] R. Thomas Eapen D. Schwab and P. Singla. Approximating admissible control onto the cislunar highways for detection and tracking of spacecraft. In *AAS/AIAA Astrodynamics Specialist Conference*, 2022.

[14] S. Fedeler, M. Holzinger, and W. Whitacre. Sensor tasking in the cislunar regime using monte carlo tree search. *Advances in Space Research*, 2022.

[15] C. Harris, D. Thomas, J. Kadan, D. Schroeder, and J. Black. Expanding the space surveillance network with space-based sensors using metaheuristic optimization techniques. In *Advanced Maui Optical and Space Surveillance Technologies Conference (AMOS)*, 2021.

[16] S. Wishnek, M. Holzinger, and P. Handley. Robust cislunar initial orbit determination, 2021.

[17] C. Channing Chow, C. Wetterer, B. Jason, M. Dilley, K. Hill, P. Billings, and J. Frith. Cislunar orbit determination behavior: Processing observations of periodic orbits with gaussian mixture model estimation filters. In *The Advanced Maui Optical and Space Surveillance Technologies (AMOS) Conference*, 2021.

[18] A. Scorsoglio L. Ghilardi and R. Furfaro. Orbit determination with maneuver estimation in cislunar environment via physics informed neural networks. In *AAS/AIAA Astrodynamics Specialist Conference*, 2022.

[19] R. Thomas Eapen M. Mayer, D. Schwab and P. Singla. Orbit characterization and determination strategies in the cr3bp framework. In *AAS/AIAA Astrodynamics Specialist Conference*, 2022.

[20] R. Broucke. Stability of periodic orbits in the elliptic, restricted three-body problem. *AIAA journal*, 7(6):1003–1009, 1969.

[21] M. Holzinger and M. Jah. Challenges and potential in space domain awareness. *Journal of Guidance, Control, and Dynamics*, 41(1):15–18, 2018.

[22] S.-S. Huang. Very restricted four-body problem. *Publications of Goddard Space Flight Center*, page 354, 1960.

[23] K.K. Boudad. *Disposal dynamics from the vicinity of near rectilinear halo orbits in the earth-moon-sun system*. PhD thesis, Purdue University, School of Aeronautics and Astronautics, 2019.

[24] A.K. de Almeida Junior and A. F. B. de Almeida Prado. Comparisons between the circular restricted three-body and bi-circular four body problems for transfers between the two smaller primaries. *Scientific Reports*, 12(1):1–19, 2022.

[25] K. Oshima. Multiple families of synodic resonant periodic orbits in the bicircular restricted four–body problem. *Advances in Space Research*, 70(5):1325–1335, 2022.

[26] R. Negri and A. Prado. Generalizing the bicircular restricted four-body problem. *Journal of Guidance, Control, and Dynamics*, 43(6):1173–1179, 2020.

[27] Y.-J. Qian, L.-Y. Yang, X.-D. Yang, and W. Zhang. Parametric stability analysis for planar bicircular restricted four-body problem. *Astrodynamics*, 2(2):147–159, 2018.

[28] S. Scheuerle Jr. Construction of ballistic lunar transfers in the earth-moon-sun system. Master's thesis, Purdue University, School of Aeronautics and Astronautics, 2021.

[29] S. Bhadauria, C. Frueh, K. Howell, and K. DeMars. Cislunar space domain awareness using bi-circular four body geometry. In *AAS/AIAA Astrodynamics Specialist Conference*, 2022.

[30] F. Sanson and C. Frueh. Noise estimation and probability of detection in nonresolved images: Application to space object observation. *Advances in Space Research*, 64:1432 – 1444, 2019.

[31] F. Sanson and C. Frueh. Quantifying Uncertainties in Signal Position in non-resolved Object Images: Application to Space Object Observation. *Advances in Space Research*, 63:2436–2454, 2019.

[32] H. Tiersch. S.B. Howell (ed.): Astronomical CCD observing and reduction techniques. Astronomical Society of the Pa-cific 1992, ASP Conference Series 23, 339 s., Preis: 55,-ISBN 0-937707-42-4. *Astronomische*

Nachrichten, 314(6):398, 1993.

[33] W.J. Merline and S.B. Howell. A realistic model for point-sources imaged on array detectors: The model and initial results. *Experimental Astronomy*, 6(1-2):163–210, 1995.

[34] H.H. Barrett, C. Dainty, and D. Lara. Maximum-likelihood methods in wavefront sensing: stochastic models and likelihood functions. *JOSA A*, 24(2):391–414, 2007.